Focal dynamics of multiple filaments: Microscopic imaging and reconstruction

P. Prem Kiran,[1,2] Suman Bagchi,[1] Siva Rama Krishnan,[3] C. L. Arnold,[4] G. Ravindra Kumar,[1] and A. Couairon[5,*]

[1]*Tata Institute of Fundamental Research, 1, Homi Bhabha Road, Mumbai 400005, India*

[2]*ACRHEM, University of Hyderabad, Gachibowli, Hyderabad 500046, India*

[3]*Department of Physics, Sri Sathya Sai University, Prasanthi Nilayam, 515134, India*

[4]*Laboratoire d'Optique Appliquée, École Nationale Supérieure des Techniques Avancées – École Polytechnique, CNRS, F-91761 Palaiseau, France*

[5]*Centre de Physique Théorique, École Polytechnique, CNRS, F-91128 Palaiseau, France*

(Received 16 October 2008; revised manuscript received 17 March 2010; published 6 July 2010)

We observe the complete dynamics of the propagation of very intense, femtosecond laser pulses in air under tight focusing conditions via direct imaging of the entire interaction zone. The whole life history of the focused pulses is then reconstructed by means of numerical simulations. We show that beam breakup leads to a dual-rate increase in filament numbers with laser power. Linearly and circularly polarized pulses give rise to beam breakup and fusion governed by external focusing conditions. For tight focusing conditions, intensity saturation due to plasma generation and nonlinear losses does not limit the intensity growth, thereby giving access to a new propagation regime featured by an efficient laser energy deposition in fully ionized air and intense 10^{15} W/cm^2 pulses at the focus.

DOI: 10.1103/PhysRevA.82.013805 PACS number(s): 42.25.Bs, 42.65.Jx, 42.65.Sf, 52.38.Hb

I. INTRODUCTION

An exciting aspect of ultrashort light pulses is the rich and complex effects they feature on propagation in a medium at high intensities. For instance, numerous properties of light filamentation constitute unique features for potential applications [1,2] such as remote secondary sources of radiation in the terahertz domain [3] and generation of few-cycle pulses and extreme ultraviolet radiation [4–6]. To date, attention has mainly been focused on long-range filament dynamics for unfocused and loosely focused (focal length >1 m) intense laser beams [7–9] for which control mechanisms were proposed [10]. Very few experimental studies have examined ultrashort laser pulse filamentation with tightly focused beams [11,12]. However, several applications require tight focusing of intense ultrashort pulses, the most remarkable among them being femtosecond laser microsurgery [13], therapy with laser-accelerated ions [14], and direct particle acceleration [15,16]. Optical "near instantaneous" techniques such as femtosecond time-resolved optical polarigraphy [17], ultrafast holography [18–21], and fluorescence imaging [22,23] can capture individual pulse events at separated spatial locations over ranges much shorter than the length of a filament. Nonoptical methods such as sonography [24] and high-voltage discharge [25], on the other hand, can provide information over entire filament lengths but with spatial and temporal resolution inferior to optical methods. In the high-power regime, direct imaging of entire filament microstructures and the complete numerical reconstruction has not been presented till now due to (a) limited spatial coverage of high-resolution optical methods, (b) lack of spatial and temporal resolution in nonoptical methods used for long filaments, and (c) the high resolution required in numerical simulations of the detailed spatiotemporal dynamics of the propagation. Experimental investigation of filamentation dynamics for tightly focused beams of powers well above the critical self-focusing threshold is thus still lacking, especially considering that it has been established that focusing conditions can significantly modify and control multiple filamentation [8].

In this paper, we address the important question of imaging and reconstructing the entire filament microstructure under tight focusing. We record *longitudinal high-resolution microscopic images* of *complete* filaments formed by individual pulses in a single frame in the focal region of highly converging focusing elements, thereby allowing an understanding of their dynamical behavior. We reconstruct the *entire* life history of tightly focused filaments by means of numerical simulations. We bring to light several novel features. The microscopic imaging of whole filaments at the geometric focus reveals a two-rate phenomenon in the growth of filament number with laser power. Imaging at higher magnification captures the detailed dynamics of the filaments. Formation of multiple filaments begins ahead of the geometric focus in the form of several premature filament microstructures. Thereafter a competition among these microstructures ensues, leading to the growth of a few mature filaments close to the propagation axis at the expense of the off-axis structures. The coherent mature filaments either form a hot spot by fusion or grow along with exchanging power. These dynamical aspects are successfully reconstructed by simulation, giving valuable insights into the role of external focusing vis-à-vis beam self-focusing. We also demonstrate that mature filaments subsequently break up into smaller and weaker filaments.

II. EXPERIMENTAL SETUP AND RESULTS

Filaments are generated from 45 fs pulses at 806 nm, 10 Hz, Ti:sapphire laser (Thales Laser, Alpha 10) with a nanosecond contrast ratio better than $10^{-6}:1$. We investigate the filaments in two different focusing geometries. Laser pulses launched in air are focused by a lens, $f = 50$ cm, leading to an $f/16$ focusing geometry in one case, and by an off-axis parabolic mirror, $f = 16$ cm, leading to an $f/6$ focusing in another. The input beam diameter before the focusing element is 30 ± 1 mm $(1/e^2)$. The imaging diagnostics include

*Corresponding author: couairon@cpht.polytechnique.fr

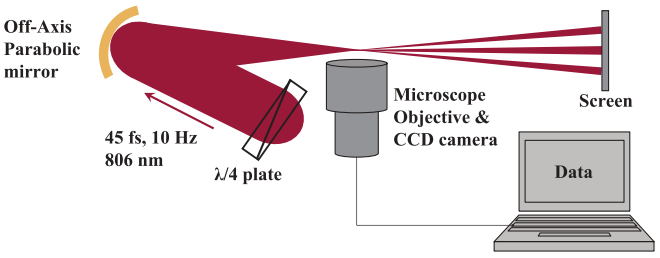

FIG. 1. (Color online) Schematic of the experimental setup showing off-axis parabolic mirror as focusing element and the diagnostic systems used.

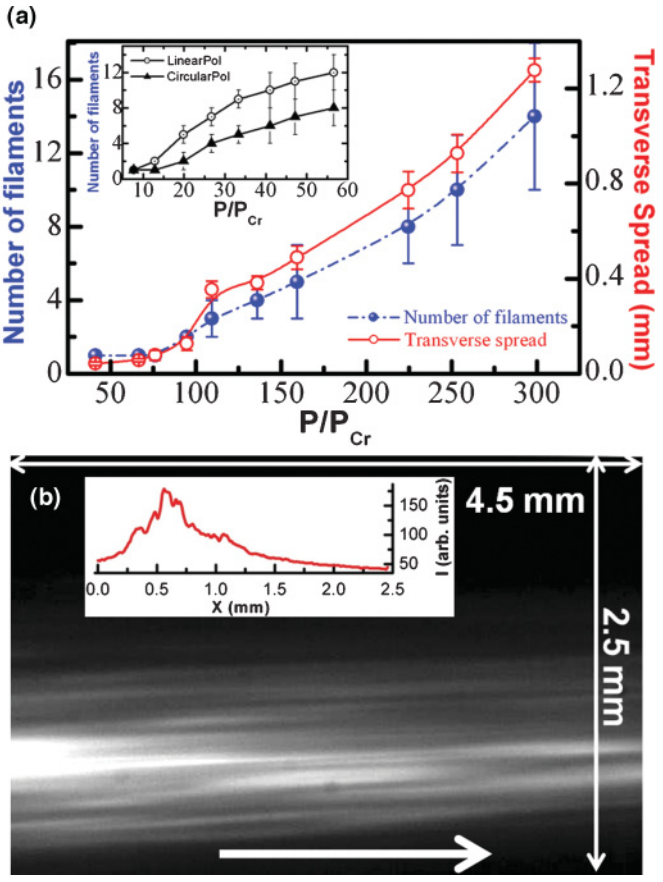

FIG. 2. (Color online) (a) Number and transverse spread of the filaments near focal plane with linearly polarized light in the (30–300)P_{cr} input power range in $f/16$ and the *inset* shows increase in filament number for linearly polarized (circles) and circularly polarized (triangles) light for the $f/6$ geometries. (b) Side view of multiple filaments for the $f/16$ geometry, linear polarization and $267P_{cr}$. The arrow shows the direction of propagation of the focused beam. The inset shows the beam profile along the x transverse direction 2.5 mm before the focus.

microscope objectives, 2× and 20×, coupled to an 8-bit charge coupled device (CCD) camera (Megaplus; Redlake ES310T). Figure 1 presents the schematic of the experiment. Filamentary structures from individual pulses were imaged. While imaging at lower magnification (2×) ensured that entire filaments were captured, the 20× imaging provided the required high resolution to image longitudinally the recombination fluorescence emitted from the entire filamentary microstructures. The laser input power is varied in the range of (40–300)P_{cr} and (6–60)P_{cr} in the $f/16$ and $f/6$ focusing geometries, respectively, where the critical power for self-focusing (P_{cr}) in air of 3 GW, smaller than the 10 GW reported in [26], was obtained from the formula $P_{cr} = 3.77\lambda_0^2/8\pi n_2 n_0$ with a nonlinear index coefficient of $n_2 = 3.2 \times 10^{-19}$ cm^2/W [27]. This value is often used in filamentation studies [1] and serves in our work as a reference scale for easy comparison to other experiments.

The number and the transverse spatial spread of filaments, defined as the full-width-at-half-maximum of individual filaments obtained from different z sections, show a quasilinear increase with input power [Fig. 2(a)] for the $f/16$ focusing geometry. By examining one-dimensional sections of the images [Fig. 2(b)] at various values of z, we defined intensity peaks smaller than 1/3 of the maximum as *premature filaments* and the rest are *mature filaments*. Mature filaments dominate the dynamics and will be the center of our attention in this discussion. For input powers greater than $60P_{cr}$ and the $f/16$ focusing geometry, we observe a drastic increase in the number of both mature and premature filaments, the rate increasing by more than a factor of 2. A maximum of 14 mature filaments were observed at $300P_{cr}$. Similar numbers were reported earlier for input powers of (42–86)P_{cr} [28] in air. The diameter of the intense mature filaments is observed to be 80 ± 10 μm till 100 P_{cr} of input power. For larger powers, the diameter is observed to be around 175 ± 25 μm. A similar trend is observed for the transverse spread of filaments. Further, the inset in Fig. 2(a) shows the increase in filament number with input powers up to $60P_{cr}$ for the $f/6$ focusing geometry. Small-scale filaments of peak intensity I_p, assumed to carry a power P_{cr}, are associated with a transverse spacing $d = \lambda_0/(2I_p n_2 n_0)^{1/2}$ [1,29], seemingly independent of the focal length. Our simulations show that in our experiments, tight focusing prevails over intensity clamping. The number of filaments thus becomes larger for tighter focusing but is limited by filament fusion and very efficient energy losses. In comparison to linearly polarized (LP) light pulses, the onset of filamentation in the case of circular polarization (CP) is delayed due to the ratio of 1.5 on the critical power for self-focusing. This results in a difference in the nonlinear focus for LP and CP with the same input power. Accordingly, the number of filaments for circular polarization is consistently smaller [inset in Fig. 2(a)], in keeping with the fact that circular polarization has been shown to suppress multiple filamentation [7]. Imaging at the lowest magnification 2× in the (40–300)P_{cr} range reveals that both the length and the transverse spread of the filaments grow with increasing laser power. The length of the filament increases from 17 to 30 mm, while the spread of the multiple filaments goes from 0.15 to 1.15 mm as shown in Fig. 2. These observations comparing the origin, size, and number of filaments from linearly and circularly polarized pulses are rendered straightforward by the present technique which therefore advantageously completes nonoptical methods [24,25].

At higher magnification, 20×, a generic life history—birth, propagation, and decay—of the filaments was observed. Figure 3(a) presents a typical case of the high-resolution image (resolution of 7 μm per pixel). Individual filaments

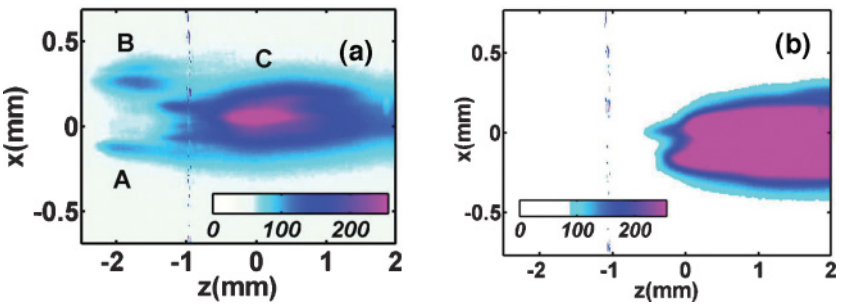

FIG. 3. (Color online) High-resolution images of the multiple filaments (side view) observed with off-axis parabolic mirror in $f/6$ focusing geometry for (a) linearly polarized pulses and (b) circularly polarized pulses at an input power of 22 P_{cr}. The line on the images is the reference used to quantify the onset of filamentation. The color bar shows the linear intensity scale inherent to the 8-bit CCD camera.

begin to appear close to the focal point. Dominant mature filaments at the center [filament C in Fig. 3(a)], having the highest power, grow at the expense of the smaller *premature* filaments [filaments A and B in Fig. 3(a)]. For circularly polarized pulses at the same power, we observed a delayed focusing, and direct formation of mature filaments is enhanced [Fig. 3(b)]. At higher powers, one or more mature filaments coherently interact, either resulting in a fusion or exchange of power seen in Fig. 2(b). In the process of propagation over several Rayleigh lengths, mature filaments undergo multiple refocusing. Filaments propagate (54–217)z_R (z_R is the Rayleigh range of the focused beam and is 141 μm in this case). Fusion, breakup, and multiple focusing of filaments over several z_R are phenomena reminiscent of the propagation features obtained in unfocused and loosely prefocused fs pulses in air at input powers $\sim 35 P_{cr}$ [30–32]. However, the dynamical behavior differs from that obtained when successive focusing-defocusing cycles are mainly driven by self-focusing. Under tight focusing conditions, external focusing plays the prevailing role with respect to the optical Kerr effect. The fusion of the filaments could not have been captured but for the direct single-shot imaging of complete filaments.

III. SIMULATIONS AND DISCUSSION OF RESULTS

For the purpose of clarifying the role of tight focusing in the multiple filamentation process, we reconstructed these observations by means of numerical simulations based on different paraxial or nonparaxial propagation models [9,13] for linearly or circularly polarized pulses [22,33], which all take the form of an unidirectional propagation equation for the Fourier components of the pulse envelope $\hat{\mathcal{E}}(k_x,k_y,\omega,z) = \mathcal{F}[\mathcal{E}(x,y,t,z)]$:

$$\frac{\partial \hat{\mathcal{E}}}{\partial z} = i[k_z(\omega,k_\perp) - k_0 - k_0'(\omega-\omega_0)]\hat{\mathcal{E}} + \mathcal{F}[N(\mathcal{E},\rho)]. \quad (1)$$

Here $k_z(\omega,k_\perp) \equiv \sqrt{k^2(\omega) - k_\perp^2}$ for the nonparaxial model, $k_z(\omega,k_\perp) \equiv \sum_{n=0}^{2} k_0^{(n)}(\omega-\omega_0)^n/n! - [k_0 + k_0'(\omega-\omega_0)]^{-1}k_\perp^2/2$ for the paraxial model, $k_\perp \equiv \sqrt{k_x^2+k_y^2}$, $k(\omega)$ represents the dispersion relation of air [34], and $k_0^{(n)} = dk/d\omega|_{\omega_0}$ at $\lambda_0 = 806$ nm. The second term on the right-hand side denotes the Fourier transform of the nonlinear terms which include plasma absorption and defocusing, nonlinear losses [$N_{NL}(\mathcal{E})$] and the optical Kerr effect [$N_K(\mathcal{E})$]:

$$N(\mathcal{E},\rho) = -\frac{\sigma}{2}(1+i\omega_0\tau_c)\rho\mathcal{E} - N_{NL}(\mathcal{E}) + N_K(\mathcal{E}) \quad (2)$$

For linear polarization, the Kerr term is given by $N_K(\mathcal{E}) \equiv i(\omega_0/c)n_2^{(LP)}I$, where $I \equiv |\mathcal{E}|^2$ and $n_2^{(LP)} = 3.2\times10^{-19}$ cm^2/W. Nonlinear losses are given by

$$N_{NL}(\mathcal{E}) = \frac{W_{PI}(I)U_i}{2I}\mathcal{E}, \quad (3)$$

where the intensity-dependent photoionization rate $W_{PI}(I)$ is calculated using the Keldysh theory (see Ref. [1] for details), and U_i denotes the ionization potential of the main ionized species (oxygen molecules in air). For circular polarization, Eqs. (1)–(3) apply to each circular component $\mathcal{E}^\pm$ with $N_K(\mathcal{E}^\pm) \equiv i(\omega_0/c)n_2^{(CP)}[|\mathcal{E}^\pm|^2 + 2|\mathcal{E}^\mp|^2]\mathcal{E}^\pm$, $n_2^{(CP)} = (2/3)n_2^{(LP)}$, and $I \equiv |\mathcal{E}^+|^2 + |\mathcal{E}^-|^2$ [7]. The inverse Bremsstrahlung coefficient $\sigma = 5\times10^{-20}$ cm^2 is calculated using the Drude theory with the collision time $\tau_c = 350$ fs. The electron density ρ was obtained by solving the rate equation

$$\frac{\partial\rho}{\partial t} = W_{PI}(I)(\rho_{air}-\rho) + \frac{\sigma}{U_i}\rho I. \quad (4)$$

As long as air remains weakly ionized, it is sufficient to only consider ionization of oxygen with $U_i = 12.1$ eV, and $\rho_{air} \simeq 5\times10^{18}$ cm^{-3} corresponds in this case to the density of neutral oxygen molecules at atmospheric pressure. Note that in the rate equation (4), the depletion of the ground state [35] is described macroscopically by the fact that the total photoionization rate $W_{PI}(\rho_{air}-\rho)$ is proportional to the time-dependent density of oxygen $(\rho_{air}-\rho)$. Equation (4) therefore accounts for depletion as well as Eq. (2) through the density ρ which saturates, but the nonlinear loss and the Kerr term in Eq. (2) do not. Our results below show, however, that important depletion occurs, because the peak intensity is high enough for single-level ionization of both nitrogen and oxygen. Our model was therefore further refined as indicated below. Equation (1) was solved by means of a standard numerical scheme based on split steps and Fourier decomposition. Tight focusing imposed the use of grids with up to 6144×6144 points in the (x,y) plane. Simulations of Eq. (1) with dispersion and only one transverse dimension as well as quasi $(3+1)$-dimensional simulations were performed without prohibitively large memory needs by using a fixed temporal shape of the pulse to integrate Eq. (4) for each grid point and account for free electron generation (frozen-time approximation). As an input beam, we used either

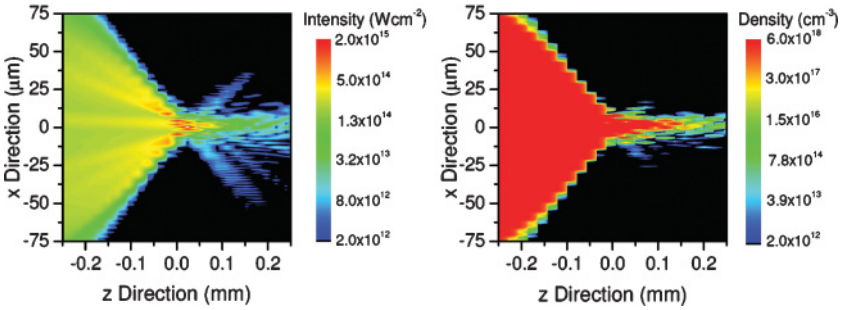

FIG. 4. (Color online) Nonparaxial simulation of multiple filamentation in the tight-focus regime with an input energy of 4 mJ and duration of 45 fs. Focusing conditions correspond to a larger numerical aperture (NA = 0.2) than in our experiments. Left column: Intensity distribution of a transverse slice ($y = 0$). Right column: Electron density distribution vs propagation distance.

the measured profile in the x direction as shown in the inset of Fig. 2(b) or we back-propagated a Gaussian beam from the focus to the starting point, 2.5 mm before the focus, by using the spherical diffraction operator, thus yielding the input profile in the y direction, which is not available experimentally. White Gaussian noise with amplitude up to 10% was then added on the input beam.

While only the results from the nonparaxial model should be expected to be quantitatively reliable, we reproduced numerically the interaction of the two initial amplitude lobes of the measured input beam, used as an initial condition of the simulation of linearly polarized pulses, for both focusing geometries and both spherical and parabolic diffraction operators. This generically led to the formation of an intermediary maximum and its subsequent decay. In the case of $f/6$ focusing with an off-axis parabolic mirror and linear polarization, the formation of initial hot spots (A and B) and their fusion at the focus to produce the mature filament (C) [see Fig. 3(a)] was retrieved. We turned off external focusing and found that the two amplitude lobes in the initial profile diverged without fusion. However, fusion is found to take place even if $n_2^{(\mathrm{LP})}$ is set, artificially, to $1/10$ of the value indicated above. Thus, external focusing prevails over the Kerr effect in the global scale dynamics of filaments, while self-focusing is important in the local dynamics exchange of power and competition between filaments.

For both the linear and the circular polarizations, the simulations revealed a rather different regime from that of standard filamentation, which we illustrate by performing calculations in the extreme case of a higher numerical aperture (NA = 0.2) as compared to our experiments (NA = 0.11): Figure 4(a) shows the dynamics of linearly polarized pulses from a sequence of intensity slices ($t = 0$, $y = 0$) around the focus as obtained from the nonparaxial model (1)–(4). Before the focus, multiple filaments grow from the inhomogeneities present in the beam. The tight focusing geometry forces the filaments to coalesce and the intensity to grow above 10^{15} W/cm^2. Figure 4(b) shows that complete ionization of oxygen is obtained well before the highest intensities are reached. Nonlinear absorption is extremely efficient: more than 99% of the energy is absorbed before the focus; however, the intensity in the focus is still 2×10^{15} W/cm^2. These levels are reduced by increasing phase noise in the input beam. We performed the same simulations without plasma defocusing and found that all intensity modulations before the focus were cleaned by multiphoton absorption. This corresponds to a new regime for which the combination of tight focusing conditions, strong nonlinear absorption, and plasma defocusing drives the intensity above a certain threshold, thereby allowing a complete ionization of the medium. This simulation result is in very good agreement with recent measurements of the electron density up to 2×10^{19} cm^{-3} for filamentation in air in similar conditions (NA = 0.11) [20] or in the range 10^{18}–10^{19} cm^{-3} for NA = 0.08 [36]. The notion of intensity saturation in standard ultrashort pulse filamentation no longer holds [37], since intensity clamping should occur at intensity levels $\sim 10^{13}$ W/cm^2 [1]. Plasma defocusing, however, plays a dominant role in the formation of small-scale filaments.

Results in Fig. 4 contain inherent approximations to the model, namely, air was treated as an oxygen gas for ionization, and depletion was not accounted for in nonlinear losses and in the optical Kerr effect, which always remained proportional to the initial neutral molecular density. We therefore checked the robustness of the results against these approximations and found that results also hold when a two-species model for oxygen and nitrogen is used. In this case, all nitrogen molecules are ionized as well, and the beam still forms a very intense hot spot at the focus. For the two-species model, Eq. (4) was replaced by rate equations for the time-dependent molecular densities ρ_{O_2} and ρ_{N_2}:

$$\frac{\partial \rho_{\mathrm{O}_2}}{\partial t} = -W_{\mathrm{PI}}^{(\mathrm{O}_2)}(I)\rho_{\mathrm{O}_2}, \tag{5}$$

$$\frac{\partial \rho_{\mathrm{N}_2}}{\partial t} = -W_{\mathrm{PI}}^{(\mathrm{N}_2)}(I)\rho_{\mathrm{N}_2}, \tag{6}$$

where, initially, air contains 20% oxygen and 80% nitrogen, i.e, $\rho_{\mathrm{O}_2}(0) = 0.2\rho_{\mathrm{air}}$ and $\rho_{\mathrm{N}_2}(0) = 0.8\rho_{\mathrm{air}}$ and in contrast to Eq. (4), here $\rho_{\mathrm{air}} \simeq 2.5 \times 10^{19}$ cm^{-3}. The electron density was calculated by $\rho(t) = \rho_{\mathrm{air}} - \rho_{\mathrm{O}_2}(t) - \rho_{\mathrm{N}_2}(t)$, which is valid as long as second-level ionization is not considered. Avalanche is no longer considered because of the shortness of the pulse durations. We also relaxed our approximation for nonlinear losses and the Kerr effect (i.e., n_2 was multiplied by $(1 - \rho/\rho_{\mathrm{air}})$, so as to describe the effect of depletion. Nonlinear losses are described by a term in Eq. (2) that is proportional to the time-dependent molecular densities ρ_{O_2} and ρ_{N_2} for a two-species model, i.e.,

$$N(\mathcal{E}) = -\frac{W_{\mathrm{PI}}^{(\mathrm{O}_2)}\rho_{\mathrm{O}_2}U_i^{(\mathrm{O}_2)} + W_{\mathrm{PI}}^{(\mathrm{N}_2)}\rho_{\mathrm{N}_2}U_i^{(\mathrm{N}_2)}}{2I}\mathcal{E}. \tag{7}$$

In the frozen-time approximation applied here, nonlinear losses would vanish as $\rho_{\mathrm{O}_2}, \rho_{\mathrm{N}_2} \to 0$ for intensities approaching complete single-level ionization. To evaluate nonlinear losses more accurately, we applied a time-averaging procedure

which amounts to extracting from the pulse energy the exact amount of energy necessary for ionization. From the evolution equation for the time-integrated intensity,

$$\frac{\partial \int_{-\infty}^{+\infty} I(t)dt}{\partial z} = -\int_{-\infty}^{+\infty} \left\{ W_{\mathrm{PI}}^{(\mathrm{O}_2)}[I(t)]\rho_{\mathrm{O}_2}(t)U_i^{(\mathrm{O}_2)} + W_{\mathrm{PI}}^{(\mathrm{N}_2)}[I(t)]\rho_{\mathrm{N}_2}(t)U_i^{(\mathrm{N}_2)} \right\} dt, \quad (8)$$

the idea of our procedure may be given by calculating the right-hand side of Eq. (8) for a square pulse of duration T_p and constant intensity I_p. In this case, the time-dependent oxygen density reads $\rho_{\mathrm{O}_2}(t) = \rho_{\mathrm{O}_2}(0)\exp\{-W_{\mathrm{PI}}^{(\mathrm{O}_2)}[I_p]t\}$, and a similar law holds for nitrogen. Equation (8) can then be directly integrated between $t = 0$ and $t = T_p$:

$$T_p \frac{\partial I_p(z,r)}{\partial z} = -\left\{ U_i^{(\mathrm{O}_2)}\rho_{\mathrm{O}_2}(0)\left[1 - \exp\left(-W_{\mathrm{PI}}^{(\mathrm{O}_2)}[I_p]T_p\right)\right] + U_i^{(\mathrm{N}_2)}\rho_{\mathrm{N}_2}(0)\left[1 - \exp\left(-W_{\mathrm{PI}}^{(\mathrm{N}_2)}[I_p]T_p\right)\right] \right\}. \quad (9)$$

From Eq. (9), we can distinguish three intensity ranges separated by the thresholds $I_{\mathrm{th}}^{(\mathrm{O}_2)}$ and $I_{\mathrm{th}}^{(\mathrm{N}_2)}$ for full ionization of oxygen and nitrogen. To quantify these thresholds, one can approximate the time-dependent oxygen density as $\rho_{\mathrm{O}_2}(t) \simeq \rho_{\mathrm{O}_2}(0)(1 - W_{\mathrm{PI}}^{(\mathrm{O}_2)}[I_p]t)$, from which $I_{\mathrm{th}}^{(\mathrm{O}_2)}$ is such that $W_{\mathrm{PI}}^{(\mathrm{O}_2)}[I_p]T_p \equiv 1$ and a similar definition holds for $I_{\mathrm{th}}^{(\mathrm{N}_2)}$.

TABLE I. Effective durations for the calculation of nonlinear losses in the model with frozen-time approximation.

	$I < I_{\mathrm{th}}^{(\mathrm{O}_2)}$	$I_{\mathrm{th}}^{(\mathrm{O}_2)} < I < I_{\mathrm{th}}^{(\mathrm{N}_2)}$	$I_{\mathrm{th}}^{(\mathrm{N}_2)} < I$
$T_i^{(\mathrm{O}_2)}$	T_p	$1/W_{\mathrm{PI}}^{(\mathrm{O}_2)}[I_p]$	$1/W_{\mathrm{PI}}^{(\mathrm{O}_2)}[I_p]$
$T_i^{(\mathrm{N}_2)}$	T_p	T_p	$1/W_{\mathrm{PI}}^{(\mathrm{N}_2)}[I_p]$

When the peak intensity is so large that one of the species is fully ionized in the leading part of the pulse, integration times shorter than the pulse duration must be used in Eq. (9) to properly account for the absorbed energy:

$$T_p \frac{\partial I_p(z,r)}{\partial z} = -\left[U_i^{(\mathrm{O}_2)}\rho_{\mathrm{O}_2}(0)W_{\mathrm{PI}}^{(\mathrm{O}_2)}[I_p]T_i^{(\mathrm{O}_2)} + U_i^{(\mathrm{N}_2)}\rho_{\mathrm{N}_2}(0)W_{\mathrm{PI}}^{(\mathrm{N}_2)}[I_p]T_i^{(\mathrm{N}_2)} \right], \quad (10)$$

where $T_i^{(\mathrm{O}_2)}$ and $T_i^{(\mathrm{N}_2)}$ denote the typical durations to be considered according to the peak intensity I_p of the pulse as indicated in Table I.

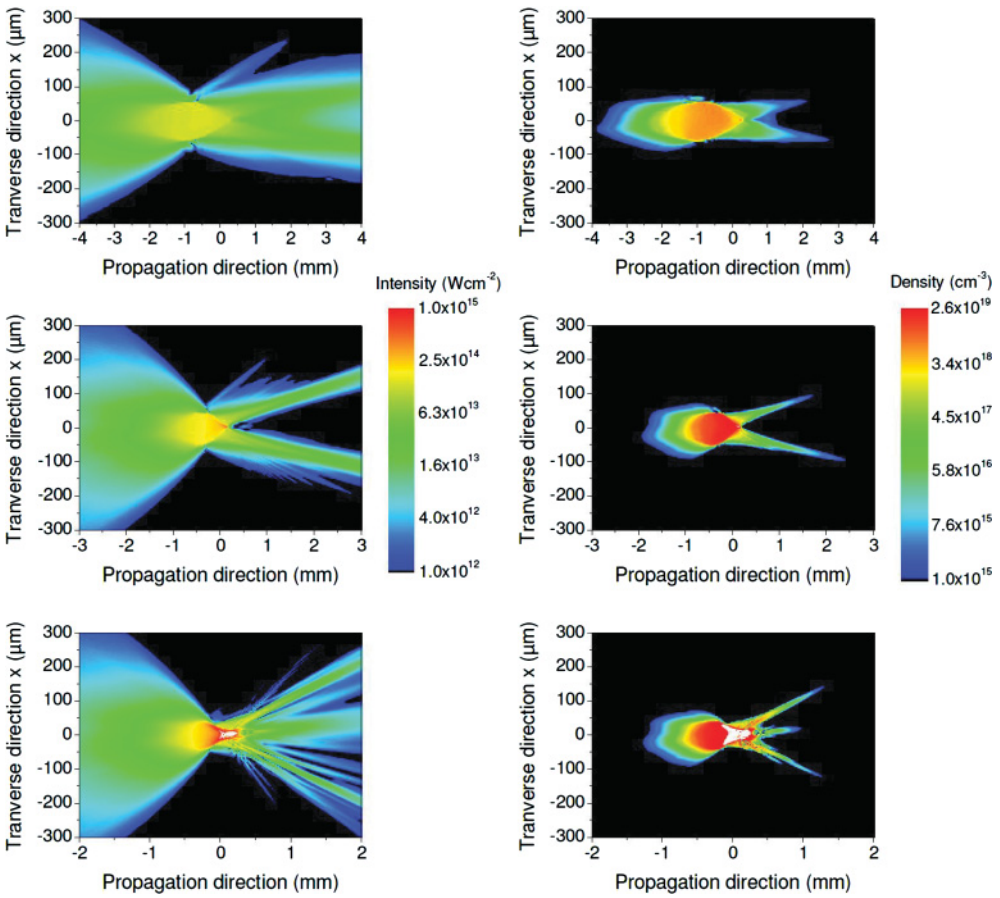

FIG. 5. (Color online) Comparison of nonparaxial simulation results for different numerical apertures. Input energy: 1 mJ; pulse duration: 45 fs. First row: NA = 0.055. Second row: NA = 0.11. Third row: NA = 0.165. First column: Intensity distribution of a transverse slice ($y = 0$). Second column: Electron density distribution vs. propagation distance. The white color close to the focus marks the region where the peak intensity exceeds 10^{15} W/cm^2 and second-level ionization starts.

A straightforward way to apply losses in Eq. (2) within the framework of our frozen-time model is thus to make the nonlinear-loss term proportional to T_i/T_p as

$$N_{\mathrm{NL}}(\mathcal{E}) = -\left[W_{\mathrm{PI}}^{(\mathrm{O}_2)}\rho_{\mathrm{O}_2}(0)U_i^{(\mathrm{O}_2)}T_i^{(\mathrm{O}_2)} + W_{\mathrm{PI}}^{(\mathrm{N}_2)}\rho_{\mathrm{N}_2}U_i^{(\mathrm{N}_2)}T_i^{(\mathrm{N}_2)}\right]\mathcal{E}/2IT_p, \quad (11)$$

where $T_i^{(\mathrm{O}_2)}$ and $T_i^{(\mathrm{N}_2)}$ are indicated in Table I. In the case of high intensities with $I > I_{\mathrm{th}}^{(\mathrm{N}_2)}$, nonlinear losses reduce to $N_{\mathrm{NL}}(\mathcal{E}) = -(0.2U_i^{(\mathrm{O}_2)} + 0.8U_i^{(\mathrm{N}_2)})\rho_{\mathrm{air}}\mathcal{E}/2IT_p$. We note that the main contribution to nonlinear losses is that occurring at high intensities, thus even a single-species model with pure nitrogen would lead to a very close expression for nonlinear losses with only 5% difference in the coefficient, expressed as $N_{\mathrm{NL}}(\mathcal{E}) = -U_i^{(\mathrm{N}_2)}\rho_{\mathrm{air}}\mathcal{E}/2IT_p$. Finally, if we had applied the above procedure to a pulse shape closer to a Gaussian, or performed an exact time integration, we would have used a shorter integration time of the order of $T_p/\sqrt{K}$, where $K = 11$ denotes the number of electrons involved in multiphoton ionization of nitrogen. The latter correction was used in our model, since nonlinear losses must be accounted for over the duration of the ionization front.

Figure 5 compares numerical results obtained for different numerical apertures covering the range or our experiments: $0.055 < \mathrm{NA} < 0.165$. The calculation is nonparaxial and accounts for the accurate description of nonlinear losses. In particular, we considered as well second-level ionization in order not to underestimate the effect of plasma defocusing, which is enhanced by second-level ionization. The simulation is initiated with the measured beam profile. For the lowest NA, the dynamics is still close to the traditional filamentation case. The intensity does not grow very high ($\sim 1.4 \times 10^{14}$ W/cm^2) and the density of free electrons is much below first-level saturation. For the experimental numerical aperture (NA = 0.11), the maximum intensity is $\sim 4 \times 10^{14}$ W/cm^2, and the density of free electrons is very close to complete first-level ionization. Finally, for the last case (NA = 0.165) traditional intensity clamping is clearly overcome. The first level is completely ionized, and the beam continues to focus. As second-level ionization starts to become efficient, there is of course additional plasma defocusing. However, the intensity easily exceeds 10^{15} W/cm^2.

Since the generation of free electrons as well as nonlinear losses were calculated by consistently considering the depletion of the medium, the relative absorption is lower, as that found in Fig. 4, for which the overestimation of nonlinear absorption reaching 99% was due to (i) the higher numerical aperture NA = 0.2, (ii) the nondepleted Kerr coefficient, and (iii) the nondepleted nonlinear absorption coefficient. A clear trend is obtained in Fig. 6: tighter focusing dissipates more power out of the beam. The relative absorption is higher for higher NA, and the amount of nonlinear absorption is above 50% of the beam even for the smaller NA. Interestingly, for the lowest NA, there is an obvious shift of the focal position toward the laser because of self-focusing, which is less strongly pronounced for higher NA. These results confirm that there is a clear transition from a regime of standard filamentation to a regime of tightly focused filamentation.

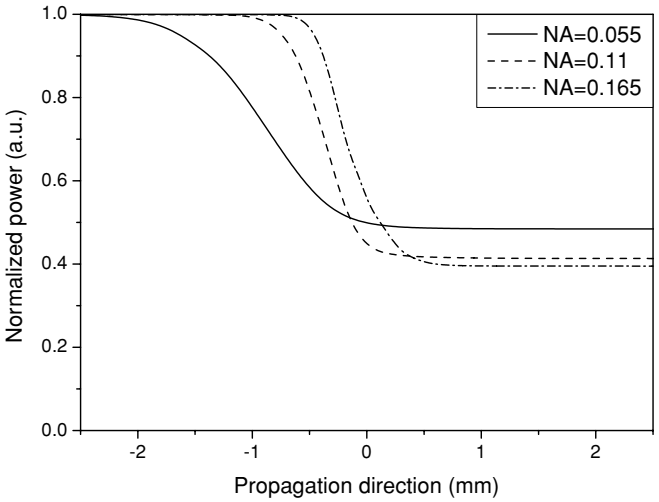

FIG. 6. Comparison of nonlinear absorption for the simulation results of Fig. 5 for three different numerical apertures. Input energy: 1 mJ; pulse duration: 45 fs.

The mechanism of this novel scenario for small-scale filamentation in tight focusing conditions is clearly illustrated by the analogy between self-focusing and the motion of a particle in a potential well, as discussed, e.g., by Shen [38]. The propagation along z of a beam of width $a(z)$ that undergoes the effects of diffraction, self-focusing, and plasma defocusing can be described by an evolution equation interpreted as governing the motion of a particle with position $a(z)$ where z plays the role of time for the particle, in a potential well $V(a) = 2(1 - P/P_{\mathrm{cr}})/k^2a^2 + \alpha/a^{2K}$ [1,39]. The first term represents the balance between diffraction and Kerr self-focusing, and the second term represents the effect of plasma defocusing where α is proportional to the ionization rate and to the density of neutral atoms. The shape of the potential is sketched in the lower part of Fig. 7 and exhibits a minimum, provided the medium is not fully ionized. Total ionization would indeed cancel the self-focusing and the plasma-defocusing terms, since both scale with the density of neutral atoms. Note also that the true evolution of the beam will differ from the motion of a particle in a potential well due to energy losses that have been neglected, therefore the purpose of this picture must be considered as a purely didactic sketch. However, the effect of energy losses is discussed below.

Standard filamentation with a loosely focused beam can be viewed as analogous to the oscillatory motion of a particle in the well, starting from a_0 without initial velocity and oscillating between a_0 and $a_{m,\mathrm{lf}}$. Plasma defocusing dominates in the falling part of the potential, whereas self-focusing prevails in the growing part. For a tightly focused beam, the initial curvature given by $(da/dz)_0$ is translated as a positive total energy in the mechanical analogy. The beam radius therefore shrinks from a_0 to $a_{m,\mathrm{tf}}$ and then increases indefinitely, similar to the case of a particle escaping from the potential well. In this situation, the effect of initial focusing (and final defocusing due to diffraction) prevails over Kerr self-focusing. The minimum beam width $a_{m,\mathrm{tf}}$ only depends on the parameters of the gas (shape of the well) and initial focusing geometry (focal distance). We now consider the effects of multiphoton absorption and of the threshold for total

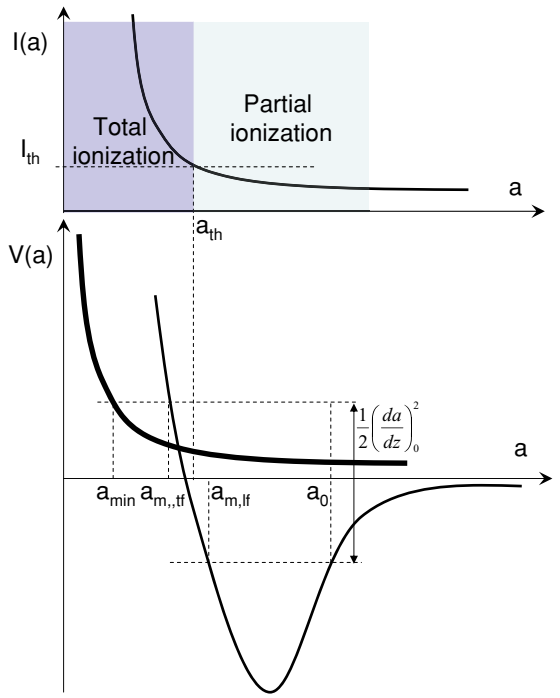

FIG. 7. (Color online) Analogy between filamentation in loose and tight focusing conditions and the motion of a particle in a potential well. Lower figure: The fine curve shows the potential well as a function of the beam width a (particle position). The bold curve shows the potential corresponding to a fully ionized medium in which plasma defocusing and Kerr self-focusing are inefficient. The filament width oscillates between a_0 and $a_{m,\mathrm{lf}}$ for a loose focusing geometry, or decreases down to $a_{m,\mathrm{tf}}$ before increasing for tight focusing conditions. Upper figure: Peak intensity vs beam width. Intensities above I_{th} and beam widths below a_{th} correspond to full ionization of the medium. In this case the filament width can decrease down to a_{min} at the focal point.

ionization I_{th}. Multiphoton absorption will induce a decrease of the beam energy, which may be viewed as the depth of the potential. Total ionization is obtained when the beam radius shrinks below a certain threshold a_{th} corresponding to an increase of the peak intensity above the threshold I_{th} (see upper part in Fig. 7) and results in switching off the effects of Kerr self-focusing and plasma defocusing (which requires a plasma channel curvature to be efficient). The potential thus becomes shaped as the bold curve in Fig. 7, which represents diffraction. Schematically, the beam radius can then decrease down to the value a_{min}, which would coincide with the geometric focus in the absence of preliminary nonlinear dynamics, and then increase due to diffraction. This sketch therefore shows that tight focusing and diffraction, i.e., linear effects, globally prevail over nonlinear effects, the role of which is limited to small-scale filamentation occurring within this global dynamics. The transition between the regimes of standard filamentation with clamped intensity and small-scale filamentation in tight focusing conditions is solely determined by the focal lens and the intensity threshold for total ionization. We finally note that intensity clamping requires a certain propagation distance to effectively lead to saturation, even in loose focusing conditions. Refocusing may occur over a shorter distance, leading to intensity spikes above the clamping intensity as observed in recent numerical simulations [6].

IV. CONCLUSION

In conclusion, we performed direct imaging of *complete* filaments in the high-intensity and tight-focusing regime and a successful numerical reconstruction of their *entire* life history. Interesting aspects of the dynamics in this regime include the dominant role of external focusing and a suppression of the phenomenon of intensity saturation, which should stimulate further investigations into the control of filaments in the tightly focused regime and the realization of possible applications relying on transport of such beams [13–16]. We provided evidence through numerical simulations of a clear transition from a standard filamentation regime with clamped intensity to a new regime of filamentation in tight-focusing conditions supported by at least single ionization of all molecules in air.

Note added in proof. Recently, we became aware of experimental results on filamentation in air with tight focusing conditions reporting intensities in the range $2–5 \times 10^{14}$ W/cm^2 and electron densities of 2.5×10^{19} cm^{-3}, in agreement with the present results [40].

ACKNOWLEDGMENTS

GRK acknowledges a DAE-SRC-ORI grant.

[1] A. Couairon and A. Mysyrowicz, Phys. Rep. **441**, 47 (2007).
[2] V. P. Kandidov, S. A. Shlenov, and O. G. Kosareva, Quantum Electron. **39**, 205 (2009).
[3] C. D'Amico, A. Houard, M. Franco, B. Prade, A. Mysyrowicz, A. Couairon, and V. T. Tikhonchuk, Phys. Rev. Lett. **98**, 235002 (2007); C. D'Amico *et al.*, New J. Phys. **10**, 013015 (2008).
[4] A. Couairon, J. Biegert, C. P. Hauri, W. Kornelis, F. W. Helbing, U. Keller, and A. Mysyrowicz, J. Mod. Opt. **53**, 75 (2006).
[5] H. S. Chakraborty, M. B. Gaarde, and A. Couairon, Opt. Lett. **31**, 3662 (2006); A. Couairon, H. S. Chakraborty, and M. B. Gaarde, Phys. Rev. A **77**, 053814 (2008).
[6] M. B. Gaarde and A. Couairon, Phys. Rev. Lett. **103**, 043901 (2009).
[7] G. Fibich and B. Ilan, Phys. Rev. Lett. **89**, 013901 (2002); Phys. Rev. E **67**, 036622 (2003).
[8] G. Méchain, A. Couairon, M. Franco, B. Prade, and A. Mysyrowicz, Phys. Rev. Lett. **93**, 035003 (2004).
[9] R. Gopal, V. Deepak, and S. Sivaramakrishnan, Pramana J. Phys. **68**, 547 (2007).
[10] L. Roso *et al.*, Appl. Phys. A **92**, 865 (2008).
[11] A. Couairon, L. Sudrie, M. Franco, B. Prade, and A. Mysyrowicz, Phys. Rev. B **71**, 125435 (2005); L. Sudrie *et al.*, Phys. Rev. Lett. **89**, 186601 (2002).
[12] F. Théberge, W. Liu, P. Tr. Simard, A. Becker, and S. L. Chin, Phys. Rev. E **74**, 036406 (2006).

[13] C. L. Arnold, A. Heisterkamp, W. Ertmer, and H. Lubatschowski, Opt. Express **15**, 10303 (2007).
[14] Y. I. Salamin, Z. Harman, and C. H. Keitel, Phys. Rev. Lett. **100**, 155004 (2008).
[15] V. Malka *et al.*, Science **298**, 1596 (2002).
[16] A. G. R. Thomas *et al.*, Phys. Rev. Lett. **98**, 095004 (2007).
[17] H. Kumagai, S.-H. Cho, K. Ishikawa, K. Midorikawa, M. Fujimoto, S. I. Aoshima, and Y. Tsuchiya, J. Opt. Soc. Am. B **20**, 597 (2003).
[18] S. Minardi *et al.*, Opt. Lett. **34**, 3020 (2009).
[19] S. Minardi, A. Gopal, M. Tatarakis, A. Couairon, G. Tamosauskas, R. Piskarskas, A. Dubietis, and P. Di Trapani, Opt. Lett. **33**, 86 (2008).
[20] D. G. Papazoglou and S. Tzortzakis, Appl. Phys. Lett. **93**, 041120 (2008).
[21] M. Centurion, Y. Pu, and D. Psaltis, J. Appl. Phys. **100**, 063104 (2006).
[22] A. Couairon, G. Méchain, S. Tzortzakis, M. Franco, B. Lamouroux, B. Prade, and A. Mysyrowicz, Opt. Commun. **225**, 177 (2003).
[23] S. A. Hosseini, Q. Luo, B. Ferland, W. Liu, N. Aközbek, G. Roy, and S. L. Chin, Appl. Phys. B **77**, 697 (2003).
[24] J. Yu, D. Mondelain, J. Kasparian, E. Salmon, S. Geffroy, C. Favre, V. Boutou, and J.-P. Wolf, Appl. Opt. **42**, 7117 (2003).
[25] S. Eisenmann, A. Pukhov, and A. Zigler, Phys. Rev. Lett. **98**, 155002 (2007).
[26] W. Liu and S. L. Chin, Opt. Express **13**, 5750 (2005).
[27] E. T. J. Nibbering, G. Grillon, M. A. Franco, B. S. Prade, and A. Mysyrowicz, J. Opt. Soc. Am. B **14**, 650 (1997).
[28] B. La Fontaine *et al.*, Phys. Plasmas **6**, 1615 (1999).
[29] V. I. Bespalov and V. I. Talanov, Zh. Eksp. Teor. Fiz. Pisma Red. **3**, 471 (1966) [JETP Lett. **3**, 307 (1966)].
[30] S. Tzortzakis, L. Berge, A. Couairon, M. Franco, B. Prade, and A. Mysyrowicz, Phys. Rev. Lett. **86**, 5470 (2001); A. Couairon *et al.*, J. Opt. Soc. Am. B **19**, 1117 (2002).
[31] S. A. Hosseini, Q. Luo, B. Ferland, W. Liu, S. L. Chin, O. G. Kosareva, N. A. Panov, N. Aközbek, and V. P. Kandidov, Phys. Rev. A **70**, 033802 (2004).
[32] Z. Hao *et al.*, Phys. Rev. E **74**, 066402 (2006).
[33] M. Kolesik, J. V. Moloney, and E. M. Wright, Phys. Rev. E **64**, 046607 (2001).
[34] E. R. Peck and K. Reeder, J. Opt. Soc. Am. **62**, 958 (1972).
[35] M. Nurhuda, A. Suda, and K. Midorikawa, New J. Phys. **10**, 053006 (2008).
[36] A. A. Ionin, S. I. Kudryashov, S. V. Makarov, L. V. Seleznev, and D. V. Sinitsyn, JETP Lett. **90**, 423 (2009).
[37] A. Couairon, Phys. Rev. A **68**, 015801 (2003).
[38] Y. R. Shen, *The Principles of Nonlinear Optics* (Wiley, New York, 2003).
[39] A. Couairon, Eur. Phys. J. D **27**, 159 (2003).
[40] X. Lu, X. L. Liu, T. T. Xi, X. Liu, and J. Zhang, "Tightly focused femtosecond laser pulse induced breakdown in air" in COFIL 2010, abstracts of the 3rd International Symposium on Filamentation, p. 73.